2023 IEEE International Conference on Robotics and Automation (ICRA 2023)
May 29 - June 2, 2023. London, UK

Dynamic Modeling and Identification of a Robotic Intracardiac Echo Catheter

Mohammad Salehizadeh† *Member, IEEE*, Filipe Pedrosa†, Harmanpreet Bassan, Rajni Patel *Life Fellow, IEEE* and Jayender Jagadeesan *Senior Member, IEEE*

***Abstract*— Catheter-based cardiac ablation is the preferred method of treating atrial fibrillation. Conventionally, the catheter is navigated in the heart using X-ray fluoroscopy imaging and an electroanatomical map. Although successful, these imaging modalities do not provide real-time feedback on the quality of lesions created, which in turn could lead to recurrence of arrhythmia. Intracardiac echo (ICE) catheter provides real-time imaging within the heart to visualize both the ablation catheter and lesions created. However, manipulating the ablation and ICE catheters simultaneously is tedious and time consuming. As a first step towards developing a robotic ICE catheter that can autonomously follow the ablation catheter and monitor the lesions, we have developed a dynamic model for the ICE catheter. The model is based on the Cosserat theory for flexible rods that relies on strain parametrization. The model also accounts for frictional forces between the catheter sheath and tendons, external loads and fluid forces acting on the catheter. A good nominal model for describing the catheter dynamics is essential to develop a robust control scheme for the robotic ICE catheter. The parameters of the ICE catheter are estimated using weight release, tendon-driven actuation and fluid flow experiments. To the best of our knowledge, this is the first dynamic model for the ICE catheter that accurately reflects the dynamics of the catheter under pulsatile fluid flow within a heart phantom.**

I. Introduction

In recent years, there has been significant research in the development of autonomous control algorithms of continuum robots including catheters for robot-assisted minimally invasive surgeries and therapies (MIST) [1]. One such application pertains to cardiac ablation to treat Atrial Fibrillation, a condition caused by ectopic beats primarily originating around the pulmonary veins [2], [3]. The navigation of the ablation catheters to burn tissue is performed under X-ray fluoroscopy or real-time intracardiac echo (ICE) imaging combined with an electroanatomical map. Although ICE-based guidance is advantageous in providing real-time information about the lesions created, it is tedious and requires simultaneous manipulation of the ablation and ICE catheters, which is nearly impossible by a single operator. There have been several papers in the literature that have reported the development of a robotic catheter for cardiac ablation [4]–[12].

Previous studies on modeling the catheter either considered the kinematics control only [13], [14] or did not consider uncertainties due to the system's varying parameters [15] and disturbances associated with a real heart environment [16]. Therefore, their resulting approaches are not necessarily robust and translatable to the clinical scenario. A myriad of approaches have been investigated for dynamic modeling and control of soft-robots and catheters. The existing body of research in this area can be broadly classified into two categories, namely: 1) Piecewise constant curvature (PCC) that represents the soft robot as a finite collection of circular arcs, which can be described by only three parameters, including radius of curvature, angle of the arc, and bending plane [17]–[22]. 2) Piecewise constant strain (PCS) [23], [24]. Compared to the PCC model, the discrete Cosserat approach taken by the PCS model can handle not only constant curvature and elongation, but also shear and torsion, which are fundamental for dealing with the strong interactions with the environment and characteristic of manipulation of the ICE catheter in the left atrium. Other works also include modeling the catheter based on the rigid-link representation [17], [25], [26].

Several researchers have also recognized the importance of modeling the non-linear dynamic forces such as friction for developing accurate control algorithm. Norouzi-Ghazbi and Janabi-Sharifi [27] have proposed a discrete friction term combined with the Cosserat rod model to account for the frictional forces acting along the backbone of the continuum catheter. Hu *et al.* [28] have also developed a kinetic model of steerable catheters by taking into account the interaction of the catheter with surrounding vasculature, however, not considering the friction forces between the tendons and the sheath of the catheter. None of the dynamic models for catheters developed thus far have considered the combined effects of both fluid flow dynamics and frictional forces to accurately describe the behavior of the catheter within the heart. This is critical for our application since the robotic ICE catheter is responsible for the real-time visualization of the ablation catheter and the surrounding heart while creating the lesions. Uncompensated motion of the ICE catheter caused by blood flow can result in jitter and motion artifacts in the ultrasound images, which may result in difficulty in monitoring the lesions created in real-time.

Our work contributes to the field by presenting a comprehensive dynamic model, identification tools, and a novel hardware setup for a robotic ICE catheter. In this paper, we

M. Salehizadeh and J. Jagadeesan are with the Department of Radiology at Brigham and Women's Hospital, and Harvard Medical School, Boston, MA 02115, USA msalehizadeh@bwh.harvard.edu

F. Pedrosa, and R. Patel are with the Canadian Surgical Technologies & Advanced Robotics (CSTAR), and the Department of Electrical and Computer Engineering, Western University, London, ON, Canada.

H. Bassan is with the Electronics Engineering Division - Accelerator Directorate, SLAC National Accelerator Lab, 2575 Menlo Park, CA 94025.

This work was supported by the NIH Grant R01EB028278 and in part by the NSERC (Canada) grant RGPIN-1345.

†M. Salehizadeh and F. Pedrosa contributed equally to this work.

base our study on the PCS model as in [23] that utilizes the continuous Cosserat's rod theory and has been shown to be sufficiently fast and accurate for the purposes of our application. As the synthesis of a robust controller requires reasonably accurate nominal parameters for the dynamic model, we have included into our dynamic model the various nonlinear effects that a catheter may experience. Furthermore, we also identify the nominal value and uncertainty range of the unknown parameters of the system using multiple catheters.

We also develop and identify *a dynamical model* of the fluid velocity behavior (with water simulating blood in our experiments) and included it as part of the overall dynamics of the robotic ICE catheter. The fluid velocity profile is compared with that of a finite element analysis and the model is validated on a patient-specific 3D printed heart phantom. Additionally, we have also integrated friction models to account for both static and sliding friction between the tendons and the catheter sheath, motor backlashes and deadzone due to slack and twist of tendons.

The underlying identification problem consists of three main steps: 1) identifying the catheter dynamics parameters using weight release experiment, 2) identifying the friction model parameters using known single-tendon actuation profiles, 3) identifying the pulsatile fluid drag parameters using a 3D printed right atrium phantom. Based on the identified dynamic model, the end goal is to devise a robust controller such as an H_∞ controller to steer the ICE catheter's distal-end in both a simulated and real heart environment with the ability to handle parameter uncertainties and disturbances as encountered in the clinical scenario. To the best of our knowledge, this is the first paper that accounts for the frictional forces along the tendons of the catheter and fluid flow dynamics to accurately model the ICE catheter dynamics within the heart phantom.

II. Catheter Dynamics model

A. Cosserat Rod Model for Catheter

We use Cosserat rod theory to express the equations of motion of a catheter [23]. Let $\boldsymbol{y} = [\boldsymbol{p}^\top\ \boldsymbol{h}^\top\ \boldsymbol{q}^\top\ \boldsymbol{\omega}^\top\ \boldsymbol{v}^\top\ \boldsymbol{u}^\top]^\top$ represent the state vector of the system, where the position, quaternion, linear and angular velocities of each segment are denoted by $\boldsymbol{p}$ and $\boldsymbol{h}$ in the global frame, $\boldsymbol{q}$ and $\boldsymbol{\omega}$ in the local frame, respectively, $\boldsymbol{R}$ gives the orientation of the local frame with respect to the base (global frame) and $(\cdot)^\top$ denotes the transpose operator. Total time horizon, sampling time, and current time are denoted by T, dt, and t. The pivotal parameters that describe the catheter dynamics are the linear and angular strains denoted by variables $\boldsymbol{v}$ and $\boldsymbol{u}$. All state variables are expressed with respect to the arc-length parametrizing variable s of the catheter ranging from proximal $s = 0$ to distal end $s = \ell$. The general dynamics of an elastic catheter rod is given by the following set of partial differential equations (PDE) [23]

$$\begin{aligned} \boldsymbol{p}_s &= \boldsymbol{R}\boldsymbol{v}, \qquad \boldsymbol{p}_t = \boldsymbol{R}\boldsymbol{q} \\ \boldsymbol{R}_s &= \boldsymbol{R}\widehat{\boldsymbol{u}}, \qquad \boldsymbol{R}_t = \boldsymbol{R}\widehat{\omega} \\ \boldsymbol{n}_s &= \rho A\boldsymbol{R}(\widehat{\omega}\boldsymbol{q} + \boldsymbol{q}_t) - \boldsymbol{f} \\ \boldsymbol{m}_s &= \partial_t(\boldsymbol{R}\rho J\boldsymbol{\omega}) - \widehat{\boldsymbol{p}}_s\boldsymbol{n} - \boldsymbol{l} \\ \boldsymbol{q}_s &= \boldsymbol{v}_t - \widehat{\boldsymbol{u}}\boldsymbol{q} + \widehat{\omega}\boldsymbol{v} \\ \boldsymbol{\omega}_s &= \boldsymbol{u}_t - \widehat{u}\boldsymbol{\omega} \end{aligned} \tag{1}$$

The material density, cross-sectional area, and second mass moment of inertia tensor of the catheter are represented by ρ, A, J while the external wrenches $\boldsymbol{f}$ and $\boldsymbol{l}$ are the distributed forces and moments acting on the sheath. The hat operator $(\cdot)^\wedge$ maps $\mathbb{R}^3$ to $\mathfrak{se}(3)$, i.e.,

$$\widehat{\omega} = \begin{bmatrix} 0 & -\omega_3 & \omega_2 \\ \omega_3 & 0 & -\omega_1 \\ -\omega_2 & \omega_1 & 0 \end{bmatrix}, \tag{2}$$

and, conversely, the wedge operator $(\cdot)^\vee$ maps $\mathfrak{se}(3)$ to $\mathbb{R}^3$. Also, subscript of s denotes derivative with respect to arc-length, subscript of t denotes time derivative. The Kelvin-Voigt model is used as the material constitutive law that acts as a linear elastic law with material damping to relate strain's displacement and curvature to internal loading. This model is expressed as

$$\begin{aligned} \boldsymbol{n} &= \boldsymbol{R}\left[k_{\mathrm{se}}(\boldsymbol{v} - \boldsymbol{v}^*) + B_{\mathrm{se}}\boldsymbol{v}_t\right] \\ \boldsymbol{m} &= \boldsymbol{R}\left[k_{\mathrm{bt}}(\boldsymbol{u} - \boldsymbol{u}^*) + B_{\mathrm{bt}}\boldsymbol{u}_t\right] \end{aligned} \tag{3}$$

where $\boldsymbol{n}$ and $\boldsymbol{m}$ are internal force and moment in the global frame respectively, k_{se} is stiffness matrix for shear and extension, k_{bt} is the bending/twisting stiffness matrix, B_{se} is the shear/extension damping matrix, B_{bt} is the bending/twisting damping matrix, $\boldsymbol{v}^* = \boldsymbol{e_3}$ is the value of the linear strain in the absence of internal forces and $\boldsymbol{u}^* = 0$ is the local curvature of a straight catheter.

In solving (1), the boundary conditions must be satisfied at both the proximal (fixed) and the distal (free) end of the catheter. At the fixed end, a subset of the state vector is known denoted by $\boldsymbol{y}_k$ and/or may be specified in terms of the actuation inputs $\boldsymbol{\tau}$, external wrenches $\bar{f}$, $\bar{l}$, and the unknown internal strains $\boldsymbol{u}$, $\boldsymbol{v}$ comprising the unknown subset $\boldsymbol{y}_u$ of the state vector at $s = 0$. The proximal boundary conditions (4) specify $\boldsymbol{p}(t,0) = \boldsymbol{p}_0$, $\boldsymbol{h}(t,0) = \boldsymbol{h}_0$, $\boldsymbol{q}(t,0) = \boldsymbol{\omega}(t,0) = 0$, while the internal strains $\boldsymbol{u}$, $\boldsymbol{v}$ are solved for by an iterative shooting method over the internal moments by leveraging (3).

$$\begin{aligned} g(0) &= \Xi\left(\boldsymbol{y}_u(0), \boldsymbol{\tau}, \bar{f}, \bar{l}\right) \\ \boldsymbol{y}_k(0) &= \xi\left(\boldsymbol{y}_u(0), \boldsymbol{\tau}, \bar{f}, \bar{l}\right) \end{aligned} \tag{4}$$

where $g(s) \in SE(3)$ defines the origin and orientation of the local coordinate frame at arc length s [29]. At the distal end of the robot $s = \ell$, there are other general boundary conditions that also must be satisfied,

$$b\left(\boldsymbol{y}(\ell), g(\ell), \boldsymbol{\tau}, \bar{f}, \bar{l}\right) = 0 \tag{5}$$

The generic functions associated with the boundary conditions above are denoted by $\Xi(\cdot)$, $\xi(\cdot)$, and $b(\cdot)$. Given that

time and space are coupled, the aim of equation (1) is to generalize the entire system dynamics expressed in space as continuous functions of arc-length s and, thus, describe the motion of the entire robot with respect to changes in the states of the system $\boldsymbol{y}$ and the actuation inputs $\boldsymbol{\tau}$ or the components of an applied wrench $\bar{f}$, $\bar{l}$ [29]. To express the time derivative of each state we use the implicit time discretization method developed by Till et al. [23] that enables one to solve robot dynamics problems at real-time rates. We call ${}^{(i)}\boldsymbol{y}_t$ *current dynamics* which contains the dynamics of the system up until the current time-step i. ${}^{(i)}\boldsymbol{y}_t$ is calculated as

$$\begin{aligned} {}^{(i)}\boldsymbol{y}_t &\approx c_0{}^{(i)}\boldsymbol{y} + \underbrace{c_1{}^{(i-1)}\boldsymbol{y} + c_2{}^{(i-2)}\boldsymbol{y} + d_1{}^{(i-1)}\boldsymbol{y}_t}_{\text{history}} \\ &:= c_0{}^{(i)}\boldsymbol{y} + {}^{(i)}{}^{h}\boldsymbol{y} \end{aligned} \tag{6}$$

Here ${}^{(i)}{}^{h}\boldsymbol{y}$ is defined as the sum of all remaining terms that rely on the past history of $\boldsymbol{y}$. The coefficients c_0, c_1, c_2, and d_1 are computed using backward differentiation formulas BDF-α method with respect to the sampling time dt, namely

$$\begin{aligned} c_0 &= \frac{1.5+\alpha}{dt(1+\alpha)} & c_1 &= -\frac{2}{dt} \\ c_2 &= \frac{0.5+\alpha}{dt(1+\alpha)} & d_1 &= \frac{\alpha}{1+\alpha} \end{aligned} \tag{7}$$

where $\alpha \in [-0.5,\ 0.0]$ interpolates between a trapezoidal and a second-order backward differentiation (BDF2) integration methods [23].

B. BVP Solution via Shooting Method

The boundary value problem (BVP) [29] is a propagation (shooting) approach that uses a nonlinear root-finding algorithm with known and unknown parameters that iteratively converges on values for the states of the system, such that the solution satisfies some boundary conditions or make the system's constraint residuals zero. The BVP technique allows both the actuator actions and the external wrench to influence every aspect of the model, including the initial conditions, the governing equations, and the boundary conditions.

The BVP of system (1) is solved via a shooting method. Since b is a function of the unknown initial conditions $\boldsymbol{y}_u(0)$, a shooting method consists of using a nonlinear root-finding algorithm, modified Newton method in our case [30], to iteratively converge on values for $\boldsymbol{y}_u$ which satisfy the boundary residuals $b = 0$. For a particular value of $\boldsymbol{y}_u(0)$, evaluation of b simply requires numerical integration of the initial value problem (4) consisting of the differential equations from $s = 0$ to ℓ , which can be computed using standard methods such as Euler, the Runge-Kutta, or Adams-Bashforth families of algorithms [29]. Now, using (1) and (3) the time derivative of each state can be expressed based on the following set of PDEs:

$$\begin{aligned} \boldsymbol{p}_t &= \boldsymbol{R}\boldsymbol{q} \\ \boldsymbol{R}_t &= \boldsymbol{R}\widehat{\boldsymbol{\omega}} \\ \boldsymbol{q}_t &= \frac{1}{\rho A}\left[k_{\text{se}}(\boldsymbol{v}_s - \boldsymbol{v}_s^*) + \widehat{\boldsymbol{u}}k_{\text{se}}(\boldsymbol{v} - \boldsymbol{v}^*) + R^\top \boldsymbol{f} - \rho A\widehat{\boldsymbol{\omega}}\boldsymbol{q}\right] \\ \boldsymbol{\omega}_t &= \frac{1}{\rho J}\left[k_{\text{bt}}(\boldsymbol{u}_s - \boldsymbol{u}_s^*) + \widehat{u}k_{\text{bt}}(\boldsymbol{u} - \boldsymbol{u}^*) + \widehat{\boldsymbol{v}}k_{\text{se}}(\boldsymbol{v} - \boldsymbol{v}^*)\right. \\ &\quad \left. + \boldsymbol{R}^\top \boldsymbol{l} - \widehat{\boldsymbol{\omega}}\rho J\boldsymbol{\omega}\right] \\ \boldsymbol{v}_t &= \boldsymbol{q}_s + \widehat{\boldsymbol{u}}\boldsymbol{q} - \widehat{\boldsymbol{\omega}}\boldsymbol{v} \\ \boldsymbol{u}_t &= \boldsymbol{\omega}_s + \widehat{\boldsymbol{u}}\boldsymbol{\omega} \end{aligned} \tag{8}$$

Terms $\boldsymbol{f}$, $\boldsymbol{l}$ encapsulate the distributed forces and moments in the global frame, respectively. Moreover, the catheter's self-weight, square law drag air resistance, and other external loads $\bar{\boldsymbol{f}}$ can be formulated as part of $\boldsymbol{f}$,

$$\boldsymbol{f} = \rho A\boldsymbol{g} - RC\boldsymbol{q} \odot |\boldsymbol{q}| - \bar{\boldsymbol{f}} \tag{9}$$

where the Hadamard product $\odot$ performs element-wise multiplication, so that

$$\boldsymbol{q} \odot |\boldsymbol{q}| := \begin{bmatrix} q_1^2\ \text{sgn}(q_1) & q_2^2\ \text{sgn}(q_2) & q_3^2\ \text{sgn}(q_3) \end{bmatrix}^\top \tag{10}$$

III. Modeling of Major Nonlinearities

A. Model of Static and Dynamic Frictional Forces

We express the total friction force as a sum of static and sliding frictional forces:

$$\boldsymbol{f}_{\text{friction}} = \boldsymbol{f}_{\text{sliding}} + \boldsymbol{f}_{\text{static}} \tag{11}$$

It is important to recognize that for an ideally flexible tendon (zero bending stiffness), the internal forces consist of only tension $\boldsymbol{\tau}_i$. As such, the internal force along the i$^{\text{th}}$ tendon, in the body frame, is modeled by:

$$\boldsymbol{n}_i^b = \boldsymbol{\tau_i}\frac{\boldsymbol{p}_{s_i}^b}{\|\boldsymbol{p}_{s_i}^b\|} \tag{12}$$

The tangential velocity of the i$^{\text{th}}$ tendon is computed as

$$\boldsymbol{\nu}_i := \frac{ds_i}{dt}\frac{\boldsymbol{p}_{s_i}^b}{\|\boldsymbol{p}_{s_i}^b\|} \tag{13}$$

We make an approximation to evaluate the static frictional force by considering only the x and y components of the internal force (in the normal and binormal directions). Moreover, the static friction should contribute only when the tangential velocity in the i$^{\text{th}}$ tendon $\boldsymbol{\nu}_i$ is zero (or below a prescribed velocity threshold). Let β_{static} denote the static coefficient of friction between the sheath and the tendons. Then, the static friction is modeled as:

$$\boldsymbol{f}_{\text{static}} = -H(\boldsymbol{\nu}_i)\beta_{\text{static}}\|(\boldsymbol{n}_i^b)_{x,y}\| \tag{14}$$

where $H(\cdot)$ is a smoothed sign function defined as $H(\cdot) := \frac{x}{\sqrt{x^2+\epsilon^2}}$, for an arbitrarily small $\epsilon > 0$. In (14), $(\boldsymbol{n}_i^b)_{x,y} = \{(n_i^b)_x,\ (n_i^b)_y,\ n_{\text{offset}}\}$. n_{offset} is theoretically expected to be zero but in practice it is a small value that needs to be identified due to the contribution of friction from

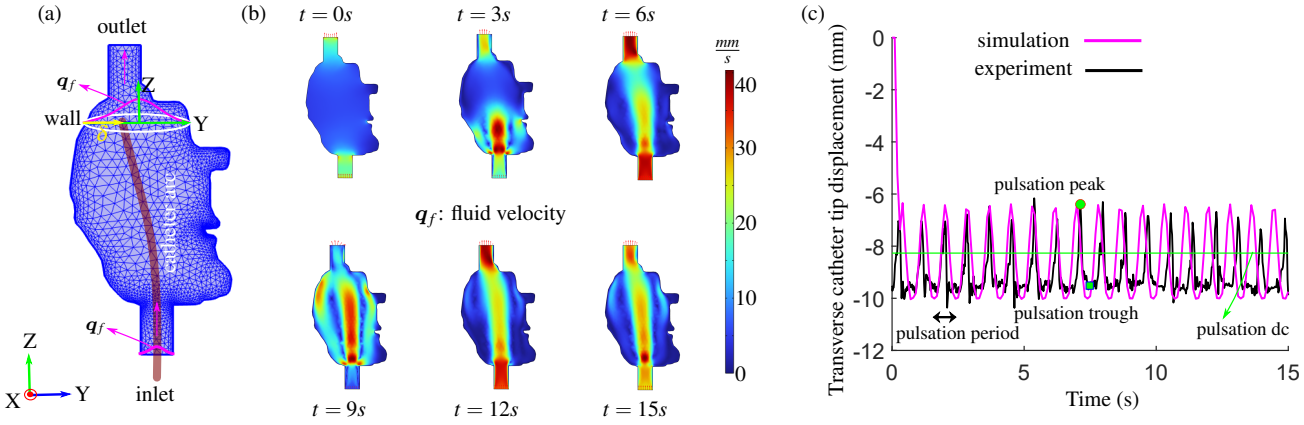

Fig. 1. (a) Mesh view of the heart's right atrium generated by finite element analysis. (b) Surface spatiotemporal fluid velocity profile. (c) Experimental versus simulated outputs using estimated parameters from identification algorithm employed to study the pulsatile fluid drag impact. The identification features are labeled.

the unmodeled section of the catheter. The inclusion of this residual n_{offset} component compensates for the catheter arc configuration in practice, which is not perfectly straight in the rest position. For the sliding frictional forces, we are interested in the x and y components of the local curvature vector as friction between sheath and tendons increases with bending curvature. Thus, the sliding friction is approximated by the following heuristics[1]:

$$\boldsymbol{f}_{\text{sliding}} = -\beta_{\text{sliding}} \boldsymbol{\tau}_i \|\boldsymbol{u}_{x,y}\| \boldsymbol{\nu}_i \tag{15}$$

Here β_{sliding} is a sliding damping coefficient, $\boldsymbol{\nu}_i$ is relative tangential velocity between the tendon i and its channel computed from past time steps, $\|\boldsymbol{u}\|$ is the magnitude of the backbone curvature, and the negative sign indicates that the frictional force is in the opposite direction to the internal tensile force in the tendon.

B. Pulsatile Fluid Drag Impact & Blood Velocity Estimation

Since the ICE catheter is navigated within the heart, it is important to model the effect of the fluid forces on the catheter dynamics. The fluid drag force exerted on a catheter is given by

$$\boldsymbol{F}_d = -\frac{1}{2}\rho_f A C_f \left[(\boldsymbol{q} - \boldsymbol{q}_f) \odot \|\boldsymbol{q} - \boldsymbol{q}_f\|\right] \tag{16}$$

where ρ_f denotes the fluid density, A is the catheter's cross-sectional area, and C_f is the Re-dependent drag coefficient. Drag coefficient is a dimensionless number, which depends upon the shape of the catheter and the Reynolds Number (Re) for the fluid flow. The wall effects result in a parabolic flow profile around the catheter. The pulsatile blood velocity is modeled by an affine combination of a time-varying periodic flow with a spatial parabolic profile $P_r(\delta)$, where δ is the algebraic distance from the catheter segment to the wall, as shown in Fig. 1(a). The pulsatile blood velocity is denoted by $\boldsymbol{q}_f(t)$. Without loss of generality, to simplify the analytical expression, we only consider the first terms of the time-varying Fourier series of the electrocardiogram (ECG) physiological pulse [31], such that

$$\boldsymbol{q}_f(t) = P_r(\delta)\left(1 + Z_f \sin\left(\omega_f t + \Phi_f\right)\right) \tag{17}$$

with spatial parabolic profile $P_r(\delta)$ approximated as

$$P_r(\delta) = a\delta^2 + b\delta + c \tag{18}$$

The parabolic profile coefficients are given by $a = -1$, $b = \frac{D}{2}$, $c = M_f + \frac{b^2}{4a}$. Here, D is the atrium diameter, M_f is the intensity peak value of the spatial profile and Z_f is the pulsation amplitude.

IV. Experimental Setup

A. Hardware Development

We have modified the Sensei robot, Hansen Medical Inc., from closed to open architecture, which gives us full access to the nine revolute and translation joints (see Fig. 2(b5)). The Sensei robot was connected to a Delta Tau motion controller and each motor was driven by a Maxon linear amplifier. The slave active module is a 10 degrees-of-freedom robotic system, which includes 7 rotational degrees of freedom and 3 translational degrees of freedom. Each axis is driven using a DC motor and feedback is provided using dual redundant incremental encoders mounted on the DC motor. In order to adapt the mechanical hardware for our research and have the ability to perform low level joint control on each axis, we used the PowerPMAC motion controller from Delta Tau Systems (now part of Omron Electronics). The motion controller utilizes a real-time Linux with Xenomai kernel and a custom motion control application that performs the servo loop control on each axis. The motion controller communicates with a high-level controller on a computer (Intel i7-4790K CPU, 4.00GHz, 16.0 GB running Windows 10) using UDP. The high-level controller runs a soft real-time multimedia timer and is responsible for generating the desired trajectory which is input to the low-level controller. We have also designed and manufactured a baseplate to connect the catheter's four tendons to four rotary motors on the

[1]The magnitude of the sliding friction should increase with the magnitude of the curvature $\boldsymbol{u}(s)$ along the normal and binormal local directions.

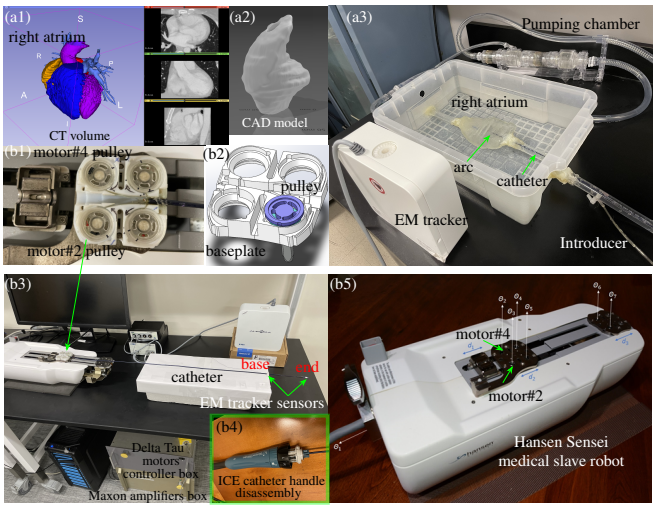

Fig. 2. (a1–a3) Steps in the construction of the heart's right atrium phantom. From (a1) 3D Slicer segmentation to (a2) 3D printing and (a3) phantom chamber fittings. (b1) and (b2) Designed and 3D printed baseplate connecting catheter tendons to the slave robot motors. (b3) View of the catheter experimental setup driven by Hansen-Medical Sensei robot and actuated using Maxon linear amplifiers and Delta Tau motor controllers. An EM tracker unit with two sensors is used. (b4) Disassembled catheter handle to access four tendons. (b5) Robot with rotary and translational motors.

slave robot (see Fig. 2 (b1, b2)). Two 5-DoF electromagnetic sensors (Northern Digital, Inc., Canada) were fixed to the base and tip of the distal bending section of the catheter to measure the real-time position and orientation of the catheter tip.

B. Heart Phantom Manufacturing

To mimic the heart chamber, we have 3D printed the right atria using a biocompatible resin (FormLabs, Inc.). The diagnostic CT images of a patient undergoing cardiac ablation were loaded in 3D Slicer, an open-source image processing software [32]. The four chambers and the pulmonary veins were manually segmented by an expert radiologist Fig. 2 (a1). In this study, we were only concerned with the right atrium. The segmented right atrium was converted to an STL model, which was then loaded into PreForm, the 3D printing software developed by FormLabs Inc., MA, for 3D printing. The 3D printed atrium was connected to an Abiomed AB 5000 circulatory support system to mimic the flow of blood through the right atrium (see Fig. 2 (a3)).

V. Results of System Identification

The main goal of identification is to determine the nominal values plus uncertainty range of unknown parameters of the dynamic model of the robotic ICE catheter. Due to high dimensionality and non-convex nature of the problem, our identification algorithm was a cascade of a global optimizer given by Multi-Level Single-Linkage (MLSL) followed by a local optimizer given by local gradient-based search algorithm for fine tuning of the optimal solution. The NLopt library [33] was used for optimization. We performed the identification experiments on five Siemens Acunav ICE catheters with 2D and 3D ultrasound sensors

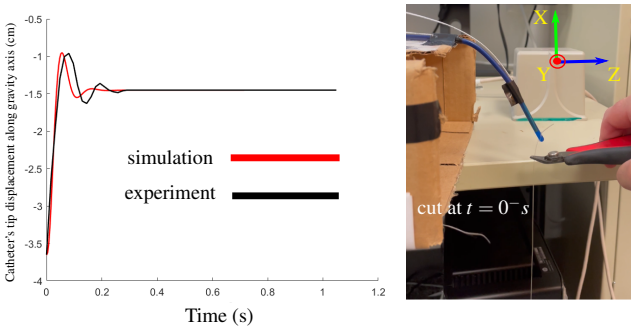

Fig. 3. Catheter's tip dynamic step response corresponding to the weight release experiment for 20grams test weight Trial #1: (red) is simulated result using the model with identified parameters. (black) is the measured response used for catheter parameters identification.

as well as different diameters. Readers are referred to the supplementary video for a detailed demo of experiments.

A. Weight Release Experiment to Identify Catheter's Characteristic Parameters

We performed weight release experiment (see Fig. 3) to identify general parameters of catheter dynamic model as presented in Table I. The optimization algorithm finds the solution for the parameters by minimizing the cost function which is a weighted ℓ_2-norm of the errors between the measured and predicted features. The general parameters of the dynamic model are comprised of density ρ, Young's modulus E, air drag coefficient C, viscous damping ratio B_{bt}, Poisson's ratio σ, and mass of the ultrasound sensor W_{us} at the tip of ICE catheter. The features include the suspended tip position d_{init} before cutting the thread attached to the test weight, the displacement after cutting the thread to reach the peak value, d_{peak}, the steady state displacement d_{ss}, three temporal features including the rise-time t_{rise}, first prominence $t_{\text{width},1^{\text{st}}}$, and first valley width $t_{\text{valley},1^{\text{st}}}$.

$$(\rho^*, E^*, C^*, B_{bt}^*, \sigma^*, W_{\text{us}}^*) = \arg\min_{x} \lambda^\top \gamma \qquad (19)$$

where the weight and parameter vectors are such that $\lambda \in \mathbb{R}_+^6$, $\gamma := \text{diag}\{\text{sgn}(x)\}x$, and the optimizing variables are $x = [\tilde{d}_{\text{init}}\ \tilde{d}_{\text{peak}}\ \tilde{d}_{\text{ss}}\ \tilde{t}_{\text{rise}}\ \tilde{t}_{\text{width},1^{\text{st}}}\ \tilde{t}_{\text{valley},1^{\text{st}}}]^\top$. To determine the nominal value of each parameter, we averaged the identified parameters over multiple trials. To determine the lower and upper bounds of the uncertain parameters we calculated minimum and maximum of the identified parameters associated with multiple trials. As demonstrated in Fig. 3, our estimated catheter tip response using the model with identified parameters is in a good agreement with the measured tip response.

B. Tendon-Driven Actuation Experiment to Identify Friction Model Parameters

We identified four friction parameters including β_{static}, β_{sliding}, n_{offset}, and ϵ as introduced in Section III-A. To this end, we actuated tendons connected to a pair of motors (motor #2 and #4) to bend catheter's tip in the vertical plane. The input signal is a time-varying smoothed $\mathcal{C}^2$ trapezoidal

TABLE I

IDENTIFICATION RESULT FOR THE WEIGHT RELEASE TRIALS WITH TEST WEIGHTS OF 5, 10, AND 20 GRAMS.

Parameters	**density** $[\mathrm{kg/m^3}]$	**Young's modulus** [G.Pa]	**air drag coefficient** $[\mathrm{kg/m^2}]$	**viscous damping ratio** [Ns/m]	**Poisson's ratio**	**US weight** [g]
Lower bound	4208	26.80	3.15×10^{-7}	3.78×10^{-6}	0.2	1.78
Nominal	6169	30.20	2.65×10^{-6}	4.93×10^{-6}	0.2	3.50
Upper bound	7881	37.80	5.06×10^{-6}	6.00×10^{-6}	0.2	5.70
Standard deviation	3223	2.90	1.42×10^{-6}	0.53×10^{-6}	0.0	0.82

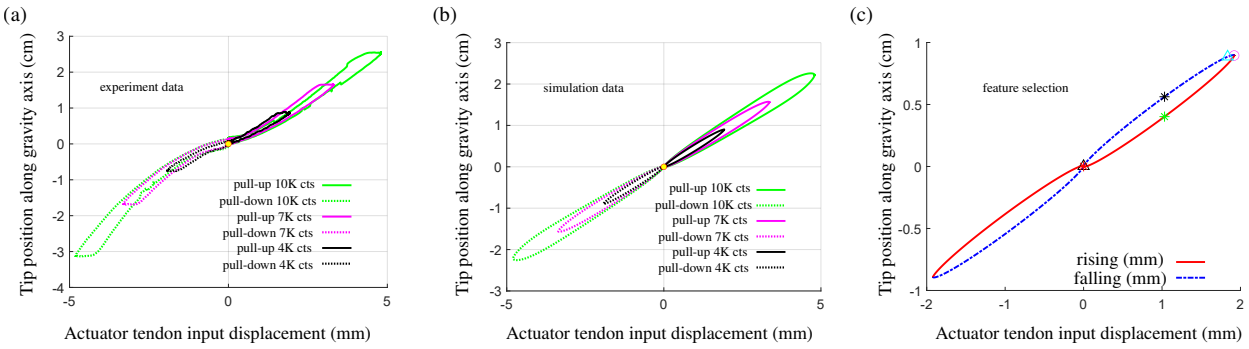

Fig. 4. (a) Experimental hysteresis profile of catheter showing the impact of friction on the motion of catheter (see the supplementary video). (b) Simulated hysteresis profile of catheter showing the impact of friction on the motion of catheter. (c) Feature selection used for identification of the friction parameters.

function. The opposite pairs of tendons were actuated to bend the catheter in a particular direction with the necessary pre-tension applied to the tendons prior to actuation.

The resulting hysteresis profile from this experiment is shown in Fig. 4(a) done for 7 trials with displacement input peaks ranging from 4000 to 10000 encoder counts (only three of them are shown here for simplicity). The features forming the friction cost function are shown in Fig. 4(c) and include the lower and upper bounds of transverse tip displacement, dead-zone width at the extremes of actuation (labeled by the magenta circle and cyan triangle), and hysteresis thickness (labeled by black and green stars). Comparing experimental hysteresis with model simulated hysteresis in Fig. 4(b), we see a reliable match in the lower and upper bounds and proportionality as the input amplitude changes.

C. Heart Phantom Experiment to Identify Fluid Drag Parameters

In this section, we describe the identification of the three fluid drag parameters, M_f, $Z_f < 1$, and C_f. The results of the identification of the fluid drag parameters are listed in Table II after being averaged for multiple catheters over multiple trials. We inserted the catheters into the 3D printed patient-specific right atrium model through the inferior vena cava (IVC) in the direction of input flow, as expected in the clinical scenario. The resultant tip displacement in the presence of pulsatile fluid flow with frequency of $\omega_f = 72$ beat per minutes (BPM) is shown in Fig. 1(c) compared with the simulated output using the identified parameters. The result shows good agreement in matching the target features, which are the mean shift in the tip position compared with the case with no fluid drag, the pulsation period, peak, and trough as labeled in Fig. 1(c). Using finite element analysis

TABLE II

ESTIMATED VALUES OF THE PARAMETERS OF THE DYNAMIC MODEL.

Symbol	**Definition**	**Nominal Value**	**Unit**
ρ	catheter density	6991	$\mathrm{kg/m^3}$
ρ_f	blood density	1060	$\mathrm{kg/m^3}$
r	cross-sectional radius	0.0041	m
ℓ	catheter arc length	13.5	cm
β_{static}	static friction coefficient	493892	N/A
β_{sliding}	sliding friction coefficient	266	N/A
ε	smoothing parameter	4.75e-6	N/A
n_{offset}	friction offset	0.0027	N
M_f	peak of fluid velocity profile	173	mm/s
Z_f	amplitude of pulsation	0.95	N/A
C_f	fluid drag coefficient	22	N/A

through COMSOL software we used 2D flow option with no-slip wall condition to quantify the spatiotemporal fluid velocity profile q_f (see Fig. 1(b)). This result matches that from the identified $M_f \simeq 173$ mm/s. The circulatory support system pumps water based on an ECG signal, as shown in Fig. 1(c). Without loss of generality in our modeling part we used a sinusoidal pulsation function as the input.

VI. CONCLUSIONS

In this paper, we have developed a dynamic model for an intracardiac echo (ICE) catheter and taken into account the various nonlinear effects such as frictional forces and fluid drag forces on the catheter. We have simulated conditions similar to those encountered within the heart during cardiac ablation procedures. This work forms the basis for developing robust control algorithm for robot-assisted control of an ICE catheter that accounts for uncertainties and disturbances present in the system.

REFERENCES

[1] P. E. Dupont, N. Simaan, H. Choset, and C. Rucker, "Continuum robots for medical interventions," *Proceedings of the IEEE*, vol. 110, no. 7, pp. 847–870, 2022.

[2] D. P. Morin, M. L. Bernard, C. Madias, P. A. Rogers, S. Thihalolipavan, and N. M. Estes III, "The state of the art: atrial fibrillation epidemiology, prevention, and treatment," in *Mayo Clinic Proceedings*, vol. 91, no. 12. Elsevier, 2016, pp. 1778–1810.

[3] M. Salehizadeh and J. Jagadeesan, "Future directions of intracardiac echocardiography (ice)," *Razminia M, Zei PC, eds. Intracardiac Echocardiography: A Handbook for Electrophysiologists*, pp. 169–179, 2022.

[4] S. B. Kesner and R. D. Howe, "Robotic catheter cardiac ablation combining ultrasound guidance and force control," *The International Journal of Robotics Research*, vol. 33, no. 4, pp. 631–644, 2014.

[5] N. Xiao, J. Guo, S. Guo, and T. Tamiya, "A robotic catheter system with real-time force feedback and monitor," *Australasian Physical & Engineering Sciences in Medicine*, vol. 35, no. 3, pp. 283–289, 2012.

[6] J. H. Crews and G. D. Buckner, "Design optimization of a shape memory alloy–actuated robotic catheter," *Journal of Intelligent Material Systems and Structures*, vol. 23, no. 5, pp. 545–562, 2012.

[7] J. W. Park, J. Choi, H.-N. Pak, S. J. Song, J. C. Lee, Y. Park, S. M. Shin, and K. Sun, "Development of a force-reflecting robotic platform for cardiac catheter navigation," *Artificial Organs*, vol. 34, no. 11, pp. 1034–1039, 2010.

[8] E. M. Khan, W. Frumkin, G. A. Ng, S. Neelagaru, F. M. Abi-Samra, J. Lee, M. Giudici, D. Gohn, R. A. Winkle, J. Sussman *et al.*, "First experience with a novel robotic remote catheter system: Amigo™ mapping trial," *Journal of Interventional Cardiac Electrophysiology*, vol. 37, no. 2, pp. 121–129, 2013.

[9] J. Jayender, R. V. Patel, and S. Nikumb, "Robot-assisted active catheter insertion: Algorithms and experiments," *The International Journal of Robotics Research*, vol. 28, no. 9, pp. 1101–1117, 2009.

[10] Y. Ganji, F. Janabi-Sharifi, and A. N. Cheema, "Robot-assisted catheter manipulation for intracardiac navigation," *International Journal of Computer Assisted Radiology and Surgery*, vol. 4, no. 4, pp. 307–315, 2009.

[11] J. Sheng, X. Wang, T.-M. L. Dickfeld, and J. P. Desai, "Towards the development of a steerable and mri-compatible cardiac catheter for atrial fibrillation treatment," *IEEE Robotics and Automation Letters*, vol. 3, no. 4, pp. 4038–4045, 2018.

[12] P. M. Loschak, Y. Tenzer, A. Degirmenci, and R. D. Howe, "A 4-dof robot for positioning ultrasound imaging catheters," in *ASME Design Engineering Technical Conference*, 2015, pp. 1–15.

[13] J. Back, L. Lindenroth, R. Karim, K. Althoefer, K. Rhode, and H. Liu, "New kinematic multi-section model for catheter contact force estimation and steering," in *IEEE International Conference on Intelligent Robots and Systems (IROS)*, 2016, pp. 2122–2127.

[14] P. Qi, H. Liu, L. Seneviratne, and K. Althoefer, "Towards kinematic modeling of a multi-dof tendon driven robotic catheter," in *36th Annual International Conference of the IEEE Engineering in Medicine and Biology Society*, 2014, pp. 3009–3012.

[15] P. M. Loschak, A. Degirmenci, C. M. Tschabrunn, E. Anter, and R. D. Howe, "Automatically steering cardiac catheters in vivo with respiratory motion compensation," *The International Journal of Robotics Research*, vol. 39, no. 5, pp. 586–597, 2020.

[16] J. Jayender, R. Patel, G. Michaud, and N. Hata, "Optimal transseptal puncture location for robot-assisted left atrial catheter ablation," *The International Journal of Medical Robotics and Computer Assisted Surgery*, vol. 7, no. 2, pp. 193–201, 2011.

[17] C. Della Santina, R. K. Katzschmann, A. Bicchi, and D. Rus, "Model-based dynamic feedback control of a planar soft robot: trajectory tracking and interaction with the environment," *The International Journal of Robotics Research*, vol. 39, no. 4, pp. 490–513, 2020.

[18] K. Xu and N. Simaan, "An investigation of the intrinsic force sensing capabilities of continuum robots," *IEEE Transactions on Robotics*, vol. 24, no. 3, pp. 576–587, 2008.

[19] R. J. Webster, J. M. Romano, and N. J. Cowan, "Mechanics of precurved-tube continuum robots," *IEEE Transactions on Robotics*, vol. 25, no. 1, pp. 67–78, 2008.

[20] K. Xu and N. Simaan, "Intrinsic wrench estimation and its performance index for multisegment continuum robots," *IEEE Transactions on Robotics*, vol. 26, no. 3, pp. 555–561, 2010.

[21] D. C. Rucker and R. J. Webster, "Parsimonious evaluation of concentric-tube continuum robot equilibrium conformation." *IEEE Trans. Biomed. Eng.*, vol. 56, no. 9, pp. 2308–2311, 2009.

[22] D. C. Rucker and R. J. Webster III, "Statics and dynamics of continuum robots with general tendon routing and external loading," *IEEE Transactions on Robotics*, vol. 27, no. 6, pp. 1033–1044, 2011.

[23] J. Till, V. Aloi, and C. Rucker, "Real-time dynamics of soft and continuum robots based on cosserat rod models," *The International Journal of Robotics Research*, vol. 38, no. 6, pp. 723–746, 2019.

[24] F. Renda, F. Boyer, J. Dias, and L. Seneviratne, "Discrete cosserat approach for multisection soft manipulator dynamics," *IEEE Transactions on Robotics*, vol. 34, no. 6, pp. 1518–1533, 2018.

[25] Y. Ganji, F. Janabi-Sharifi *et al.*, "Catheter kinematics for intracardiac navigation," *IEEE Transactions on Biomedical Engineering*, vol. 56, no. 3, pp. 621–632, 2009.

[26] M. Khoshnam, A. C. Skanes, and R. V. Patel, "Modeling and estimation of tip contact force for steerable ablation catheters," *IEEE Transactions on Biomedical Engineering*, vol. 62, no. 5, pp. 1404–1415, 2015.

[27] S. Norouzi-Ghazbi and F. Janabi-Sharifi, "Dynamic modeling and system identification of internally actuated, small-sized continuum robots," *Mechanism and Machine Theory*, vol. 154, pp. 1–13, 2020.

[28] X. Hu, L. Cao, Y. Luo, A. Chen, E. Zhang, and W. Zhang, "A novel methodology for comprehensive modeling of the kinetic behavior of steerable catheters," *IEEE/ASME Transactions on Mechatronics*, vol. 24, no. 4, pp. 1785–1797, 2019.

[29] D. C. Rucker and R. J. Webster, "Computing jacobians and compliance matrices for externally loaded continuum robots," in *IEEE International Conference on Robotics and Automation*, 2011, pp. 945–950.

[30] R. Bulirsch and J. Stoer, *Introduction to Numerical Analysis*. Springer, 2002, vol. 3.

[31] L. Arcese, M. Fruchard, and A. Ferreira, "Endovascular magnetically guided robots: navigation modeling and optimization," *IEEE Transactions on Biomedical Engineering*, vol. 59, no. 4, pp. 977–987, 2011.

[32] A. Fedorov, R. Beichel, J. Kalpathy-Cramer, J. Finet, J.-C. Fillion-Robin, S. Pujol, C. Bauer, D. Jennings, F. Fennessy, M. Sonka *et al.*, "3d slicer as an image computing platform for the quantitative imaging network," *Magnetic Resonance Imaging*, vol. 30, no. 9, pp. 1323–1341, 2012.

[33] S. G. Johnson and J. Schueller, "Nlopt: Nonlinear optimization library," *Astrophysics Source Code Library*, pp. ascl–2111, 2021.